Boundary-layer instability measurements on a cone at freestream Mach 3.5

Rudolph A. King,[1, a)] Amanda Chou,[1] Ponnampalam Balakumar,[1] Lewis R. Owens,[1] and Michael A. Kegerise[1]

Flow Physics and Control Branch, NASA Langley Research Center, Mail Stop 170, Hampton, VA 23681-2199, USA

(Dated: 28 September 2021)

An experimental study was conducted in the NASA (National Aeronautics and Space Administration) Langley Supersonic Low-Disturbance Tunnel to investigate naturally-occurring instabilities in a supersonic boundary layer on a 7° half-angle cone at nominal freestream conditions: Mach 3.5, total temperature of 299.8K, and unit Reynolds numbers (millions per m) of 9.89, 13.85, 21.77, and 25.73. Instability measurements were acquired under noisy-flow and quiet-flow conditions. Pitot-pressure and calibrated hot-wire measurements were obtained using a model-integrated traverse system to document the model flow field. In noisy-flow conditions, growth rates and mode shapes achieved good agreement between the measured results and linear stability theory (LST). The corresponding N factor at transition from LST is $N \approx 3.9$. Under quiet-flow conditions, the most unstable first-mode instabilities as predicted by LST were measured, but this mode was not the dominant instability measured in the boundary layer. Instead, the dominant instabilities were less-amplified, low-frequency disturbances predicted by LST, and grew according to linear theory. These low-frequency unstable disturbances were initiated by freestream acoustic disturbances through a receptivity process believed to occur near the branch I location of the cone. Under quiet-flow conditions, the boundary layer remained laminar up to the last measurement station for the largest unit Reynolds number, implying a transition N factor of $N > 8.5$.

[a)] Author to whom correspondence should be addressed: rudolph.a.king@nasa.gov

I. INTRODUCTION

The accurate prediction of laminar-to-turbulent transition on vehicles in atmospheric flight still remains a challenge today, more than a century after the seminal work of Reynolds.[1] For high-speed flows, boundary-layer transition can dramatically influence the aerodynamic behavior of slender reentry vehicles. To develop more accurate physics-based transition prediction tools that are also practical for use early in the vehicle design phase (i.e., a focus on LST), there is a need for quantitative off-body flow-field measurements in test environments resembling flight conditions. These detailed measurements are generally acquired in ground-based tunnels, but these facilities can present difficulties with the interpretation of test results at high-speed test conditions. Confusing test results only serve to add uncertainties in high-speed vehicle aerodynamic performance prediction capabilities.

Boundary-layer transition is highly sensitive to many environmental conditions. These environmental effects enter the boundary layer through a receptivity[2] process and can ultimately lead to early transition and vehicle performance degradation. Fedorov[3] applied numerical and asymptotic analysis to study the receptivity process and showed that acoustic waves synchronize with boundary-layer modes near the leading-edge region. This is problematic in supersonic and hypersonic wind tunnels where the dominant source of freestream disturbances (i.e., tunnel noise) for Mach numbers greater than 3 is acoustic radiation from turbulent boundary layers and roughness/waviness on the tunnel nozzle walls (e.g., Laufer[4] and Pate and Schueler[5]). As such, design engineers need to be judicious in interpreting and extrapolating transition results acquired in conventional ground-based facilities to flight. A review of the effects of high-speed tunnel noise on boundary-layer transition is given in an article by Schneider.[6] For a freestream Mach number of 3.5, Chen, Malik, and Beckwith[7] demonstrated experimentally that boundary-layer transition on a flat plate and a cone at zero incidence is significantly influenced by changing the freestream noise level. They showed that transition Reynolds numbers under low-noise conditions increased by as much as a factor of three on a cone and by a factor of seven on a flat plate, as compared to conventional wind-tunnel data. Their results are consistent with flight data.

For a flat plate and a cone at zero incidence, LST predicts that the dominant instabilities in supersonic flow are first-mode oblique instabilities (see Mack[8]). To better understand the instability mechanisms that lead to transition in supersonic flow, unsteady off-body mea-

surements are desired in boundary layers with thicknesses that are on the order of 1 mm or less (limited by available tunnel size). Most measurements in previous research were made using uncalibrated hot-wire anemometry in flat-plate boundary layers. Researchers[9–14] report supersonic stability results on flat plates using natural or forced excitation in conventional wind tunnels. Studies that applied controlled excitation[9,10,13] generally agreed with compressible LST. Measurements made with a natural wind-tunnel freestream environment [11,12,14] revealed instability growth at frequencies not predicted by LST. Kendall[11] found low correlation levels between the freestream sound and boundary-layer fluctuations for $M = 1.6$ and 2.2. As Mach number increased from 3 to 5.6, the correlation between the freestream and boundary-layer fluctuations increased, confirming that the freestream sound field drove the boundary layer. The boundary-layer fluctuations at low values of R_l (Reynolds number based on Blasius length scale, $l = \sqrt{\mu x/(\rho u)}$) were more consistent with the forcing theory of Mack[15]. At $M = 3$, Demetriades[12] found that disturbances causing transition began growing monotonically at all frequencies and were not predicted by LST. He measured evidence of first-mode instability predicted by linear theory, but these disturbances played a very minor role in the transition process. More recently, Graziosi and Brown[14] acquired calibrated hot-wire measurements on a flat plate at $M = 3$ with relatively low freestream noise levels that were realized in a conventional tunnel by operating at very low total pressures. Good agreement was found between measured growth rates of the high-frequency unstable waves and theory, but linear theory did not predict the measured growth of the low-frequency disturbances.

For cones at zero incidence, stability measurements at supersonic speeds are less available. Corke, Cavalieri, and Matlis[16] reported on preliminary instability measurements with uncalibrated hot wires in the boundary layer of a 7° half-angle cone in NASA Langley's Supersonic Low-Disturbance Tunnel (SLDT). They introduced controlled disturbances near branch I (lower neutral point) using a plasma actuator array under quiet-flow conditions and measured the development downstream. A pair of helical waves was excited in the most-amplified band of frequencies and wave angles. These measurements were extended by Matlis[17] using the same cone model and test facility, with a hot-wire calibrated to mean mass flux. The excited mode was amplified downstream and maintained a constant azimuthal spanwise mode number (i.e., the wave angle of the oblique modes decreased with downstream distance). Without excitation in the quiet-flow environment, no instabilities were

measured in the boundary-layer at the test conditions; however, he measured boundary-layer disturbances under noisy-flow conditions. Recent work[18] investigated first-mode instability waves in a natural disturbance environment of a conventional wind tunnel on a 7° half-angle cone at Mach 3. Measured growth rates and spectra from wall-mounted pressure sensors compared well with LST. The agreement between uncalibrated hot-wire results and linear theory was not as good. Growth rates were significantly underpredicted by linear theory, and peak frequencies of the first-mode waves were overpredicted by linear theory.

More recently at the NASA Langley Research Center, we have invested considerable effort to make calibrated off-body measurements in our SLDT at Mach 3.5 on flat-plate, cone, and wedge-cone models. We have acquired measurements that compare favorably with computational results.[19–23] Details of our approach are given in Kegerise, Owens, and King.[19]

The objective of this study was to improve our physical understanding of the supersonic laminar-to-turbulent transition process by studying the naturally-occurring disturbances in a transitioning boundary layer in a low-disturbance environment simulating flight disturbance levels. The measurements obtained in this study are likely to extend our knowledge beyond that achieved in the earlier cone studies[7,24] in this low-noise facility, which were based on mean surface measurements. This was done by meticulously characterizing the freestream and boundary-layer edge incoming conditions, documenting the baseline cone flow, and measuring the boundary-layer disturbances as they developed downstream. Computational fluid dynamics (CFD) simulations of the mean flow and LST computations were performed at the nominal test conditions.

An in-depth complementary analysis that considered the forced-response outcomes based on these measurements are presented by the current authors.[25] Computations were performed for the main test condition of the current cone experiment to understand the observed evolution of disturbances inside the boundary layer. Freestream noise was generated to mimic nonuniform radiated noise from the nozzle walls as measured in our experiment by placing harmonically oscillating blowing and suction sources at the surface of the nozzle. The acoustic field radiated from this source was obtained by solving the linearized Euler equations. The computed acoustic field was superimposed on the outer boundary of the computational domain that lies outside the bow shock formed on the cone. Time-accurate simulations were performed to investigate the generation and evolution of disturbances inside

the boundary layer at different frequencies, convection speeds, and azimuthal wavenumbers. More details will be provided later in this article.

In §II, we discuss the experimental details and approach of the study. In §III, a brief overview of the computational approach is provided. Results are presented in §IV where measured results are compared to computational results. A discussion is given in §V followed by a brief summary in §VI.

II.   EXPERIMENTAL DETAILS

A.   Facility and model

The study was conducted using the Mach 3.5 axisymmetric nozzle in the NASA Langley Supersonic Low-Disturbance Tunnel (SLDT). The SLDT is a blowdown wind tunnel that utilizes large-capacity, high-pressure air on the upstream end and large vacuum systems on the downstream end. The low-noise design is achieved by increasing the extent of laminar boundary-layer flow on the nozzle walls. To extend the laminar nozzle-wall flow of the axisymmetric nozzle, a three-pronged approach[26] is utilized: 1) the removal of the upstream turbulent boundary layers from the settling chamber just upstream of the throat, 2) the slow expansion of the nozzle contour, and 3) the highly-polished surface finish of the nozzle walls. The upstream boundaries of the uniform low-noise test region are bounded by the Mach lines that delineate the uniform Mach 3.5 flow. The downstream boundaries of the low-noise test region are formed by the Mach lines that emanate from the acoustic origin locations, i.e., the locations where the nozzle-wall boundary layers transition from laminar to turbulent flow as depicted in figure 1. The tunnel is capable of operating in a low-noise ("quiet") or in a conventional ("noisy" or "high-noise") test environment when the bleed-slot valves are opened or closed, respectively. With the bleed-slot valves opened, the upstream turbulent boundary layers are removed at the bleed slot located just upstream of the nozzle throat. The extent of the quiet test core depends on the value of freestream unit Reynolds numbers Re_∞, with larger quiet test regions associated with lower values of Re_∞. Under quiet-flow conditions with bleed-slot valves opened, the normalized freestream static-pressure fluctuation levels are found to be $\langle P'_\infty \rangle / \bar{P}_\infty < 0.1\%$. Here $(\bar{\ })$, $(\ )'$, and $\langle\ \rangle$ denote the mean value, unsteady component, and rms value, respectively. With the bleed-slot valves closed,
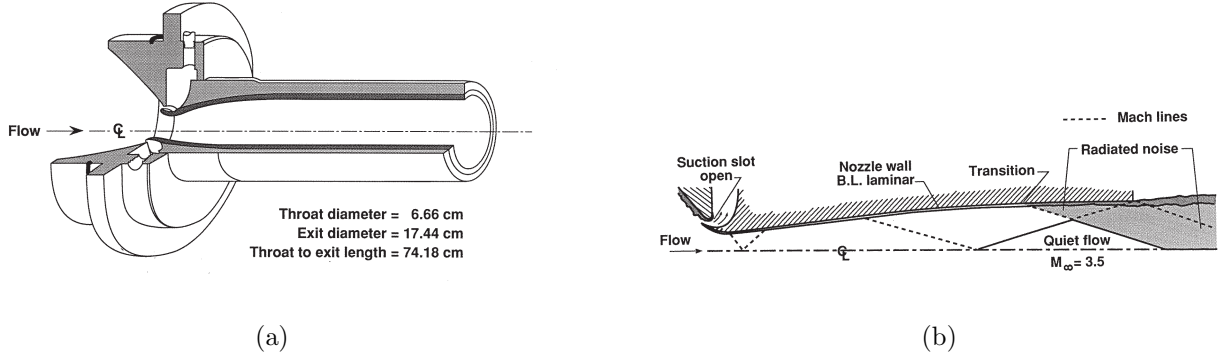
FIG. 1. Mach 3.5 axisymmetric nozzle: (a) isometric cutaway view and (b) schematic depicting quiet test core.

the upstream turbulent boundary layers are allowed to continue into the nozzle. Under noisy-flow conditions with the bleed-slot valves closed, the pressure fluctuations are found to be consistent with conventional tunnels, i.e., typically in the range of $0.3 < \langle P'_\infty \rangle / \bar{P}_\infty < 1\%$. Measured Mach-number profiles and $\langle P'_\infty \rangle / \bar{P}_\infty$ for a range of tunnel total pressures in the axisymmetric nozzle are reported by Chen, Malik, and Beckwith.[26] The axisymmetric nozzle has an exit diameter of 17.44 cm. The typical operational envelope of the tunnel is a freestream Mach number of $M_\infty = 3.5$, a maximum total pressure of $P_0 = 1.38$ MPa, and a maximum total temperature of $T_0 = 366$ K. A complete description of the tunnel is given by Beckwith et al.[27]

The test model is a 7° half-angle cone that is 381 mm in length with a nominally sharp nose tip (tip radius ≈ 0.05 mm). The model is comprised of a large replaceable nose tip and an aft frustum that mates at 190.5 mm from the cone apex. The model is highly polished with an estimated surface finish of 0.1 μm rms. The model is instrumented with ten static pressure orifices (0.508 mm diameter) that are located along a ray on the cone frustum (between $s = 228.6$ mm and 342.9 mm with a spacing of 12.7 mm where s is measured along the cone surface from the apex). Surface temperatures on the model are measured using six type-K thermocouples located at $s = 76.2, 101.6, 127, 254, 292.1$ and 330.2 mm. The thermocouples are secured to the backside of the model surface. The three upstream thermocouples are located in the cone tip portion of the model and the latter three in the cone frustum.

A three-axis model-integrated traverse is used to provide probe movement in the wall-normal (y, pitch of the probe head), downstream (s, parallel to the cone surface), and
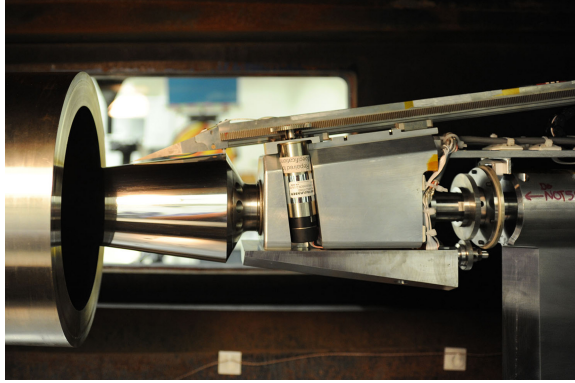
6

FIG. 2. Cone model installed in SLDT. Diffuser capture not installed for this image.

azimuthal ϕ directions. The traverse rack is aligned to the cone surface (see figure 2 for a picture of the cone model installed in the tunnel). The starting point for the model traverse design and the probe tip design to follow were based on previous research by Corke et al.[16] The leading edge of the traverse arm—just downstream of the probe attachment location— is preloaded with a teflon foot that slides on the cone surface. This mitigates unwanted vibrations under aerodynamic loading and damage to the cone surface finish when the arm is cantilevered forward. The s-axis motion along the cone surface is provided by a rack and pinion system and is driven by a miniature stepper motor. The travel extent along the cone for this test is $120 \leq s \leq 300$ mm. The s-axis resolution is 0.081 mm, based on laser-tracker measurements used to evaluate the accuracy of this motion. The azimuthal motion is achieved using a spur gear configuration, where the larger gear is fixed on the model sting and the smaller gear rotates with a counterbalanced block located just downstream of the cone base. This motion is also driven by a miniature stepper motor. The total range of motion in the azimuthal-axis direction is $-125° \leq \phi \leq 125°$ where $\phi = 0°$ is top dead center. An encoder provides position feedback in the azimuthal direction and is mounted to the model sting. The encoder accuracy is estimated to be $\sim \pm 0.1°$. The wall-normal motion is achieved by pivoting the probe head about a pivot point that is driven by a lead screw and miniature stepper motor. The relative rotational motion of the probe head is measured with a differential variable reluctance transducer (DVRT) displacement sensor. A calibration procedure was performed for each probe head that relates the translational motion of the DVRT displacement sensor to the relative locations of the probe-tip (see Kegerise, Owens, and King[19] for details on the calibration procedure). The range of travel for the wall-normal
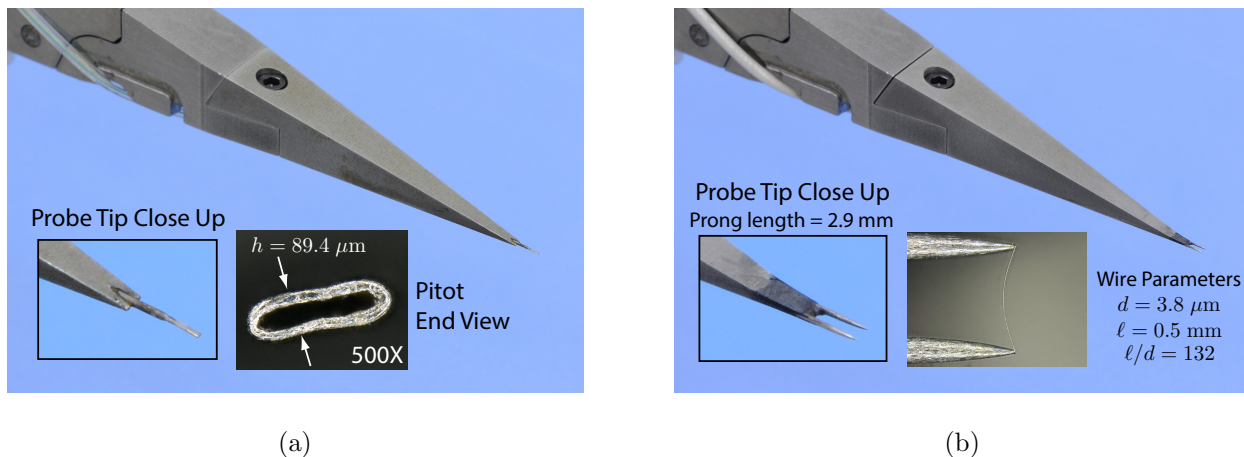
FIG. 3. Photographs of the boundary-layer probes and relevant dimensions: (a) pitot probe and (b) hot-wire probe.

motion from the model surface is $y \approx 4$ mm. The y-axis probe positions are capable of being set to within ± 6.5 μm for the boundary-layer surveys. More details of the cone model and integrated traverse are provided by Owens, Kegerise, and Wilkinson.[22]

B. Probes and instrumentation

Cone surface pressures and temperatures were monitored and measured throughout the test campaign. The ten static surface pressures were measured with 34.5 kPa differential transducers utilizing an electronic pressure scanning system with a stated accuracy of 0.03 % full scale. The reference pressure was acquired with a 13.33 kPa absolute gauge that has a stated accuracy of 0.05 % reading. The six surface temperatures were acquired using a thermocouple measurement card with integrated signal conditioning. The stated accuracy of the system for the type-K thermocouples used is 0.36 °C.

Mean pitot-pressure data were acquired in the cone boundary layer using a wedge-shaped pitot probe that was mounted on the three-axis model-integrated traverse system. A photograph of the probe is shown in figure 3(a). For the pressure data, the pitot tube was flattened to have a frontal area with an approximate width and height of 285.03 μm and 89.42 μm (open area approximately 258.45×39.62 μm), respectively (see insets in figure 3(a)). The pitot probe was connected to an ultraminiature pressure transducer using a 0.508-mm I.D. tubing. The small "dead" volume (1.485 mm^3) of the pressure transducer and the small volume of the tubing helped to minimize the settling time for the pitot probe. The typical

stated accuracy of the transducer is 0.1 % full scale.

Mean total-temperature data were acquired with the wedge-shaped hot-wire probes (figure 3(b)) across the boundary layer. These are later referred to as cold-wire surveys, in contrast to the traditional hot-wire surveys. For these measurements, the hot-wire probe was disconnected from the anemometer and connected to a precision 6.5-digit digital multimeter on a 100-ohm range for resistance measurements. The wire sensor resistance was then converted to total temperature (see discussion below in §II C).

Mean and unsteady mass-flux data were acquired with single-element hot-wire probes operated in a constant-temperature mode with a 1:1 bridge configuration. Two types of hot-wire anemometry measurements were acquired: 1) in the cone flow field to measure the boundary-layer flow field and 2) in the empty tunnel to obtain freestream mass-flux measurements. The former measurements were acquired using a wedge-shaped hot-wire probe, as shown in figure 3(b), that was mounted on the model-integrated traverse system. These boundary-layer hot-wire measurements represent the bulk of the reported data. The wire sensors used for the boundary-layer measurements were platinum-plated tungsten wires with sensor diameters of $d = 3.8$ μm and lengths of $l = 0.5$ or 1 mm. Typical response bandwidths of the boundary-layer hot wires were estimated based on the traditionally-accepted square-wave-injection response to be in excess of 310 and 290 kHz for the 0.5 and 1-mm long wires, respectively. As stated earlier, previous work[16] was used as the starting point for the boundary-layer probe body design. Subsequent CFD and experimental analysis on the wedge-shaped probe body was conducted to further minimize the boundary-layer flow interference and details are provided by Owens, Kegerise, and Wilkinson.[22] The AC-coupled hot-wire output of the boundary-layer probe from the anemometer was conditioned with a low-noise amplifier/filter before being digitized with a 16-bit A/D (analog-to-digital) converter at a rate of 1 MHz and a total of 2×10^6 sample points. Programmable gain was applied by the amplifier/filter system to maximize the dynamic range of the A/D. The signal was high-pass filtered with a 4-pole, 4-zero filter at 1 kHz (to reduce the vibrational response associated with the model-integrated traverse system) and antialias filtered with a 6-pole, 6-zero filter at 400 kHz.

Additionally, hot-wire measurements were acquired in the tunnel freestream with an empty test section using the tunnel traverse. The hot-wire probes for these measurements were standard normal single-wire probes with $d = 5$ μm and $l = 1.25$ mm. The sensing

elements here were also platinum-plated tungsten wires. The response bandwidths for the freestream probes typically exceeded 220 kHz. As with the boundary-layer anemometer signal, the AC-coupled output for the freestream probe was also conditioned with a low-noise amplifier/filter system before being digitized with the 16-bit A/D converter at 0.5 MHz and a total of 1×10^6 sample points. Programmable pre- and post-gain were applied by the amplifier/filter system to maximize the dynamic range of the A/D converter. These signals were AC coupled at 0.25 Hz and antialias filtered with an 8-pole, 8-zero filter at 200 kHz. For all hot-wire measurements, the anemometer was operated at high overheat ratios, $\tau = 0.8$ or 0.9, so that the wires were sensitive primarily to mass flux, ρu (where ρ and u are the density and velocity, respectively). The mean hot-wire data were DC coupled and low-pass filtered at approximately 100 Hz before being acquired by a precision 6.5-digit digital multimeter on a 10-volt range for voltage measurements.

An electronic fouling circuit was designed to indicate when the probe first made contact to the model surface. Before each profile measurement (pitot or hot wire), the probe was electrically fouled on the model surface to set the y-axis location. This was achieved by slowly moving the probe (a few steps at a time) towards the wall until the pitot tip for the pitot probe and the prongs for the hot-wire probe made contact to the model surface. The probe was then retracted so that the probe just became unfouled with the surface. Using the DVRT calibration data referenced earlier and the position offset data (distance from the model surface to the center of the sensor location when fouled), the y-axis locations were estimated. More details on this process are given by Kegerise, Owens, and King.[19]

C.   Data reduction

Mach-number boundary-layer profiles were obtained from the pitot-pressure measurements. The average value of the ten static surface pressures on the cone surface was used as an estimate of the edge static pressure. This pressure agreed well with the Taylor-Maccoll conical-flow solution for a 7° half-angle cone. Using both the measured pitot pressure and the average surface pressure, we solved for the Mach number by applying the isentropic relations in the subsonic regime and the Rayleigh pitot tube formula in the supersonic regions.

The hot-wire reduction analysis was limited to $M > 1.2$, where the Nusselt number becomes independent of Mach number. We followed the approach used by Smits et al.[28]

by operating the wires at large overheats ($\tau > 0.5$), $\tau = (T_w - T_r)/T_0$, so that the wire responded primarily to mass flux. The temperatures T_w and T_r are the wire temperature and wire recovery temperature, respectively. The calibration equation was reduced to the form:

$$E_b^2 = A + B(\rho u)^n, \tag{1}$$

where A, B, and n are the calibration constants that were obtained from a least-squares curve fit, and E_b is the uncorrected bridge voltage. Hot-wire calibrations were conducted in SLDT either on the nozzle centerline with an empty test section or downstream of the conical shock with the model installed. The calibrations were performed at a nominally fixed total temperature, T_c, corresponding to our test conditions ($T_c = 299.8 \pm 0.6$ K) and at the low tunnel pressure conditions to match the local wire Re conditions in the boundary layer.

A temperature correction to the anemometer bridge output was necessary to account for local variations in $T_0(y)$ relative to T_c across the boundary layer, hence we applied a temperature correction $\sqrt{T_0/T_c}$ to the output bridge voltage E_b. The relevant hot-wire equation to apply across the boundary layer now becomes

$$E_b^2(T_0/T_c) = A + B(\rho u)^n. \tag{2}$$

Examples demonstrating the validity of this approach were presented in an earlier paper.[19] In order to estimate $T_0(y)$ across the boundary layer, a cold-wire survey was always acquired with each hot-wire survey. For the cold-wire survey, the sensor resistance was measured at each wall-normal location. With the wire sensor submerged in the flow stream, the wire temperature equilibrates to the recovery temperature T_r ($= \eta_r T_0$). The wire recovery factor η_r has been shown to depend on both the wire Reynolds number, $\rho u d/\mu_0$ (where μ_0 is the dynamic viscosity evaluated at T_0), and Mach number. For supersonic Mach numbers, the recovery factor is independent of Mach number.[29,30] The recovery factor is generally independent of the wire Reynolds number for $\rho u d/\mu_0 > 20$.[31,32] However, for the current test, wire Reynolds numbers less than 20 were realized in the lower region of the boundary layer. The cold-wire calibrations were performed over the same mass-flux range as the hot-wire calibrations for each probe. The cold-wire calibration entailed measuring the wire sensor recovery resistance r_r and the tunnel total temperature (nominally constant). The wire recovery temperature was estimated using a linear resistance-temperature relationship,

namely

$$T_r = \frac{r_r - r_{ref}}{\alpha r_{ref}} - T_{ref}. \tag{3}$$

Here, α (=0.0036 K^{-1}) is the temperature coefficient of resistance and r_{ref} and T_{ref} are the reference resistance and temperature near ambient conditions, respectively. The recovery factor was then estimated using $\eta_r = T_r/T_0$, which is a function of the wire Reynolds number.

The subsequent mass-flux data reduction in the boundary layer is an iterative process since we do not know the η_r in advance. We begin by making an initial guess for η_r to compute T_0. Equation 2 is evaluated using the measured mean bridge voltage $\overline{E}_b$ and T_0 to get the mean mass flux $\overline{\rho u}$. An updated value of η_r is evaluated from the cold-wire calibration using the most recent value of $\overline{\rho u}$ and T_0 to update the wire Reynolds number. This process is continued until a satisfactory convergence of both $\overline{\rho u}$ and T_0 is achieved with the most recent values. This iterative process is done for all the boundary-layer measurement stations. The mean and unsteady bridge voltages are then combined to give the instantaneous value, $E_b = \overline{E}_b + E'_b$. Now that $T_0(y)$ is known across the boundary layer, the instantaneous mass flux ρu is obtained using Eq. 2 for each measurement station. The instantaneous mass flux is then decomposed into its mean and unsteady components, $\rho u = \overline{\rho u} + (\rho u)'$. All power spectral densities, $G_{\rho u}(f)$, were estimated using Welch's method, where f is frequency. Each sample record was divided into 400 equal segments. Fifty percent overlapping was used and a Hanning data window was applied to each data block. The frequency resolution for all $G_{\rho u}$ presented is 200 Hz.

Narrowband rms mass flux with bandwidths of $\Delta f_{bw} = 5$ kHz were computed to estimate the measured disturbance mode shapes and disturbance amplification growth rates within selected frequency bins. These rms mass-flux values are identified by the center frequency $f_c = 5, 10, 15, ..., 100$ kHz, and the energy is integrated over a frequency band of $f_c - \Delta f_{bw}/2 \leq f < f_c + \Delta f_{bw}/2$. The mass-flux mode shapes at a given s station are the $\langle(\rho u)'\rangle$ values at the desired f_c. The boundary-layer disturbance growth at a desired f_c is obtained by selecting the maximum mode-shape value at f_c for each s location. A curve fit for the maximum $\langle(\rho u)'\rangle$ versus s can be computed for each value of f_c, i.e., twenty curve fits for twenty f_c values. We then denote the curve-fit functions as $\tilde{A}_{f_c}(s)$ such that an estimate of the spatial amplification growth rate is given as

$$-\alpha_i = \frac{1}{\tilde{A}_{f_c}} \frac{d\tilde{A}_{f_c}}{ds}. \tag{4}$$

An exponential function raised to the power of a second-order polynomial was used as the curve-fit model for $\tilde{A}_{f_c}(s)$. This functional form was selected because the physical growth rate based on linear theory is exponential. This provides for three curve-fit constants that were obtained by minimizing the square of the residuals. Goodness-of-fit metrics (e.g., summed square of residuals, correlation of determination, and rms error) were evaluated for the curve fits and were found to be acceptable.

III.   COMPUTATIONS

The computations were performed over a 7° half-angle cone at the nominal test conditions of the experiment. The axisymmetric unsteady compressible Navier-Stokes equations in conservation form are solved in the computational curvilinear coordinate system. The viscosity is computed using Sutherland's law and the coefficient of conductivity is written in terms of the Prandtl number. The governing equations are solved using a fifth-order accurate weighted essentially nonoscillatory (WENO) scheme for space discretization and a third-order, total-variation-diminishing (TVD) Runge-Kutta scheme for time integration.

The outer boundary of the computational domain lies outside the shock and follows a parabola. This ensures that the boundary-layer growth is accurately captured. At the outflow boundary, an extrapolation boundary condition is used. At the wall, viscous no-slip conditions are used for the velocity boundary conditions. The wall temperature condition is prescribed as a constant adiabatic temperature (268.2 K) near the nose tip ($s < 51$ mm) and is gradually followed by a linear wall temperature distribution that increases to 278.9 K at $s = 300$ mm. This wall temperature distribution is employed based on measurements of the six surface temperatures after the model is thermally conditioned (see discussion by Owens, Kegerise, and Wilkinson[22]). The density at the wall is computed from the continuity equation. In the mean-flow computations, the freestream values at the outer boundary are prescribed. The steady mean flow is computed by performing unsteady computations using a variable time step until the maximum residual reaches a small value ($\sim 10^{-11}$). A CFL number of 0.2 is used. Details of the algorithm solution and computational approach are given by Balakumar, Zhao, and Atkins,[33] and Balakumar.[34,35]

Spatial stability analyses were performed on the computed mean-flow states at different streamwise locations. For this paper, the analysis is limited to parallel linear stability theory

13

TABLE I. Nominal freestream and edge unit Reynolds numbers for the test conditions ($M_\infty = 3.5$, $T_0 = 299.8$ K). For the calculation of R_l, s is in units of mm.

P_0, kPa	$Re_\infty \times 10^{-6}$, m^{-1}	$Re_e \times 10^{-6}$, m^{-1}	R_l	Tunnel State
172.4	9.89	11.12	$105.44\sqrt{s}$	Quiet
241.3	13.85	15.57	$124.76\sqrt{s}$	Noisy
379.2	21.77	24.46	$156.40\sqrt{s}$	Quiet
448.2	25.73	28.91	$170.02\sqrt{s}$	Quiet

computations and focused on oblique first-mode instabilities. The form of disturbances used to perform the stability computations is given by

$$q(y, s, \phi, t) = \tilde{q}(y) \exp^{i(\alpha_r s + m\phi - 2\pi f t) - \alpha_i s} \tag{5}$$

where q is the disturbed flow variable, α_r is the streamwise wavenumber, and m is the azimuthal wavenumber (integral number of azimuthal waves around the cone circumference). Analysis details of the LST computations are given by Balakumar.[35,36] Mean-flow CFD and LST results are compared to experimental results in the following section.

IV. RESULTS

The results to follow will be discussed for a few test conditions. All data were acquired with a nominal freestream Mach number of $M_\infty = 3.5$ and nominal total temperature of $T_0 = 299.8$ K. To aid the reader, the test conditions are tabulated in table I. Our discussions will mostly reference conditions with respect to P_0 and s, so this table will help the reader to navigate quickly between (P_0, s) variables and (Re_∞, Re_e, R_l) variables. Re_e is the unit Reynolds number based on boundary-layer edge conditions and $R_l = \sqrt{Re_e s}$, which is the Reynolds number based on the Blasius length scale.

In the discussion to follow, we refer to the electronic noise as the minimum detectable level that the anemometry system was capable of measuring, i.e., the anemometer noise floor. We employed best practices to minimize the electronic noise. This electronic noise level should not be confused with low-noise or high-noise level of the tunnel flow as this refers to the radiated aerodynamic noise environment. Consequently, one noisy-flow condition was tested

at $P_0 \approx 241.3$ kPa to evaluate our approach, as we expected to obtain excellent SNR (ratio of measured anemometry signal to the anemometry electronic noise) of the unsteady hot-wire measurements for these conditions. However, our main goal was to acquire measurements in the *natural* low-noise environment of the tunnel, knowing that we would have signal levels at least an order of magnitude smaller than those for the noisy-flow case, resulting in reduced SNR.

We know from past experience in low-speed work[37,38] that receptivity and stability experiments are very sensitive to the state of the mean flow and environmental conditions. As a result, we exercised extreme care to carefully document the mean flow and environmental conditions to avoid ambiguous results as reported by Nishioka and Morkovin[39] and Saric.[40] We first present results on the freestream conditions and boundary-layer edge conditions downstream of the conical shock to evaluate our environmental conditions. Then, the mean flow is documented and compared with the computational results to establish the baseline flow conditions. Finally, we examine the measured stability characteristics and reconcile with the LST results.

A.   Freestream and boundary-layer edge measurements

Before installing the model, freestream hot-wire measurements were acquired along the nozzle centerline to assess the low-noise performance of the repolished Mach-3.5 axisymmetric nozzle. Data were acquired over a range of total pressures to evaluate the extent of laminar flow on the nozzle walls. We were able to achieve laminar flow just beyond $P_0 = 450$ kPa, which was less than the value of $P_0 \approx 630$ kPa reported by Chen, Malik, and Beckwith.[26] However, we did improve the low-noise performance of the prepolished nozzle, which was limited to $P_0 \approx 241.3$ kPa.

One future goal in our prediction toolkit is to be able to predict transition location reliably with an amplitude-based method. To that end, knowledge of the amplitude and spectral content of the incoming unsteady disturbances is essential. Consequently, an attempt was made here to document the unsteady flow field in the freestream and boundary-layer edge. First, hot-wire data were acquired along a vertical centerline plane in an empty test section to include $450.85 \leq X \leq 927.10$ mm and $-50.8 \leq Y \leq 50.8$ mm in 6.35 mm increments in both directions. The tunnel coordinates X and Y are measured in the streamwise direction
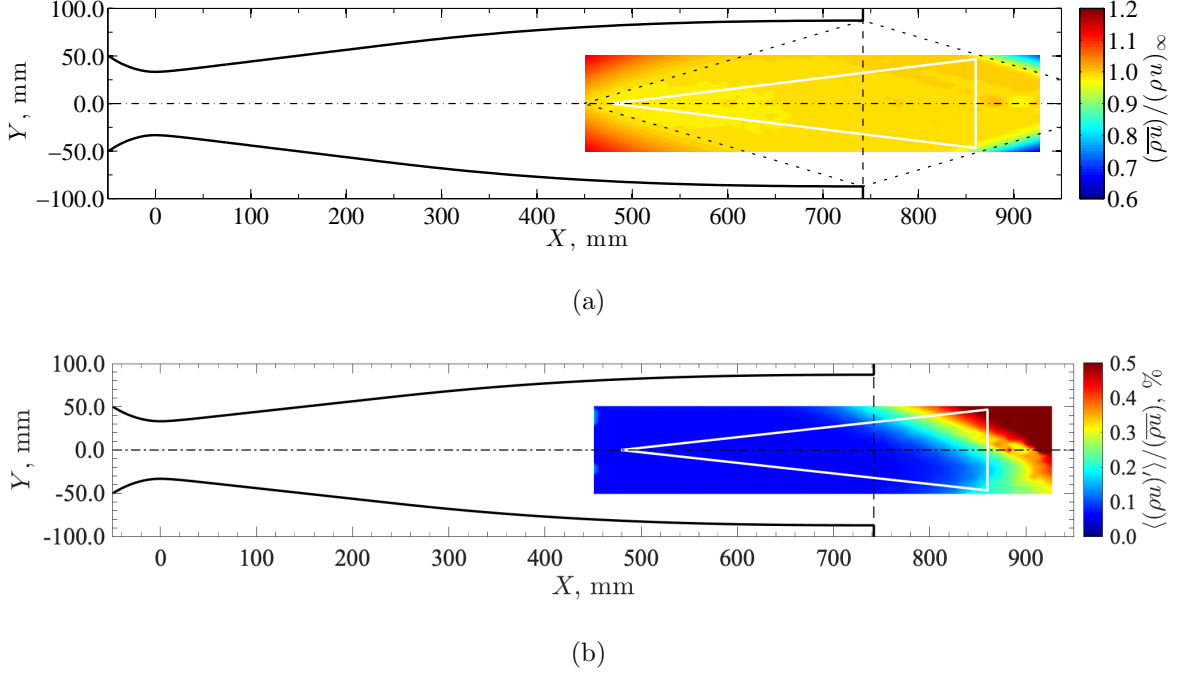
FIG. 4. Contours of measured mass flux in the empty nozzle under quiet-flow conditions for $P_0 \approx 174.6$ kPa: (a) $(\overline{\rho u})/(\rho u)_\infty$, and (b) $\langle(\rho u)'\rangle/(\overline{\rho u})\%$. The solid white line depicts the cone location in the following measurements.

from nozzle throat and in the vertical direction from nozzle centerline, respectively. Mass-flux results for $P_0 \approx 174.6$ kPa are shown in figure 4 in the form of contour plots. The plots also include lines that delineate the cone model (solid white line) if it was present, the nozzle contour (solid black line), the nozzle exit location (dashed line), and the uniform-flow test region (short-dashed lines). The measured mean mass flux normalized by the calculated freestream mass flux, $(\overline{\rho u})/(\rho u)_\infty$, is presented in figure 4(a). The accompanying unsteady rms mass flux normalized by the measured mean mass flux, $\langle(\rho u)'\rangle/(\overline{\rho u})$, is shown in figure 4(b). Parts of the upstream and downstream sections of the uniform-flow test region are visible in the mean mass-flux contours. Meanwhile, the percent rms mass-flux contours clearly show that most of the cone resides in the quiet test core, i.e., where $\langle(\rho u)'\rangle/(\overline{\rho u}) < 0.1\%$. Figure 4(b) also reveals that the nozzle-wall boundary-layer transition is not symmetric—boundary-layer transition on the upper nozzle wall precedes transition on the lower wall. Similar plots are presented in figure 5 for $P_0 \approx 452.0$ kPa (near the maximum achievable quiet-flow conditions). The mean mass-flux plots for both tunnel conditions are very uniform and consistent. The transition location on the nozzle wall moves forward for
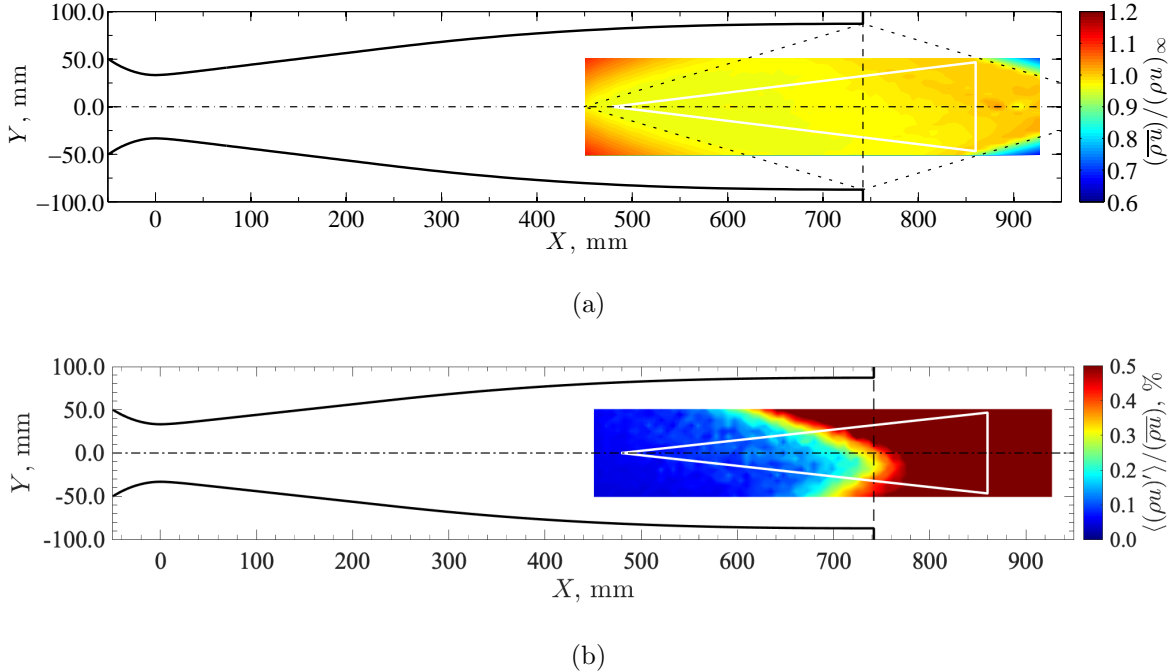
16

(a)

(b)

FIG. 5. Contours of measured mass flux in the empty nozzle under quiet-flow conditions for $P_0 \approx 452.0$ kPa: (a) $(\overline{\rho u})/(\rho u)_\infty$, and (b) $\langle(\rho u)'\rangle/(\overline{\rho u})\%$. The solid white line depicts the cone location in the following measurements.

the higher pressure as expected. The asymmetry of the transition front is still apparent. This asymmetry was always present, even after successive cleaning attempts of the nozzle. Even at the highest tunnel pressure for quiet flow, it is important to note that more than 50% of the cone resided in the quiet test core (see figure 5(b)).

The normalized broadband rms mass flux for empty-tunnel freestream data are compared to boundary-layer edge data in figure 6. The rms mass flux $\langle(\rho u)'\rangle$ is integrated over a 100 kHz bandwidth. The boundary-layer edge data were acquired outside the boundary layer at $y \approx 2$ mm along the s-axis direction and are shown as unfilled symbols. The empty-tunnel freestream data are extracted from the data shown in figures 4(b) and 5(b) based on the closeness in proximity of the (X, Y) location to the (s, y) location of the boundary-layer edge data. Datasets are normalized by the local $(\overline{\rho u})$, i.e., $(\overline{\rho u})_\infty$ or $(\overline{\rho u})_e$. For the data at $P_0 \approx 175$ kPa (figure 6(a)), the boundary-layer edge data at $\phi = 0°$ show that the flow is quiet all the way to the last measurement station ($s = 300$ mm), unlike the empty-tunnel data, which begins to increase at $s \approx 230$ mm. We believe this discrepancy occurred due to a change in the nozzle quiet-flow performance—the nozzle was cleaned on multiple occasions
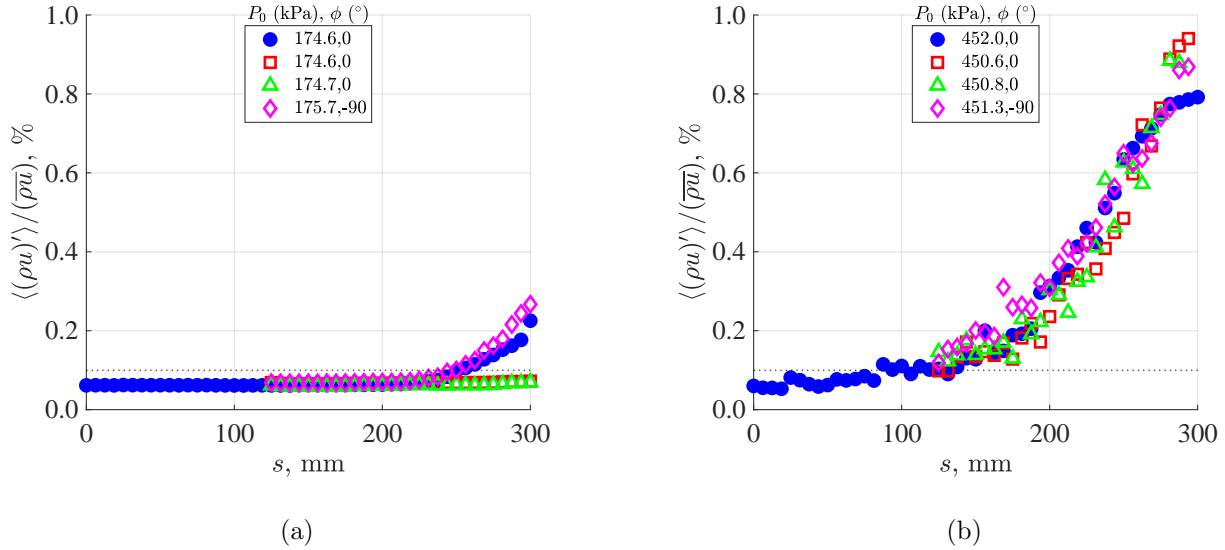
17

FIG. 6. Normalized rms mass-flux fluctuation under quiet-flow conditions with (unfilled symbols) and without (filled symbols) the cone model in the test section: (a) $P_0 \approx 175$ kPa, and (b) $P_0 \approx 450$ kPa. The dotted line represents the 0.1% level.

(over a period of 5.5 months) between the empty-tunnel measurements and the subsequent boundary-layer edge measurements with the model. The noise level at $\phi = -90°$ for the boundary-layer edge data also shows an increase at a similar location as the empty-tunnel data. This trend in the boundary-layer edge data at $\phi = -90°$ versus the values at $\phi = 0°$ is also observed at $P_0 \approx 379.2$ kPa (data not shown). Figure 6(b) shows a similar plot for the largest Re_∞ condition. The first half of the cone is in a quiet environment where the fluctuation levels are approximately 0.1% or less. The data in figure 6 demonstrate that the presence of the model and associated conical shock does not have an adverse effect on the normalized $\langle (\rho u)' \rangle$ measurements. Recall also that the empty-tunnel data and boundary-layer edge data were acquired with different probe bodies, wire sensor diameters and lengths, and traverse systems as discussed in §II B.

Next, we examine the spectral content of the data in figure 6. Figure 7 shows power spectral densities at three selected locations—one just upstream of the cone tip (empty-tunnel data only) and the other two at $s \approx 125$ and 250 mm, where both empty-tunnel data and boundary-layer edge data exist. Electronic noise data obtained from wind-off conditions are also shown for both sets of measurements. These are representative of the anemometer system noise for all test conditions and show characteristic f-squared noise. Consequently,
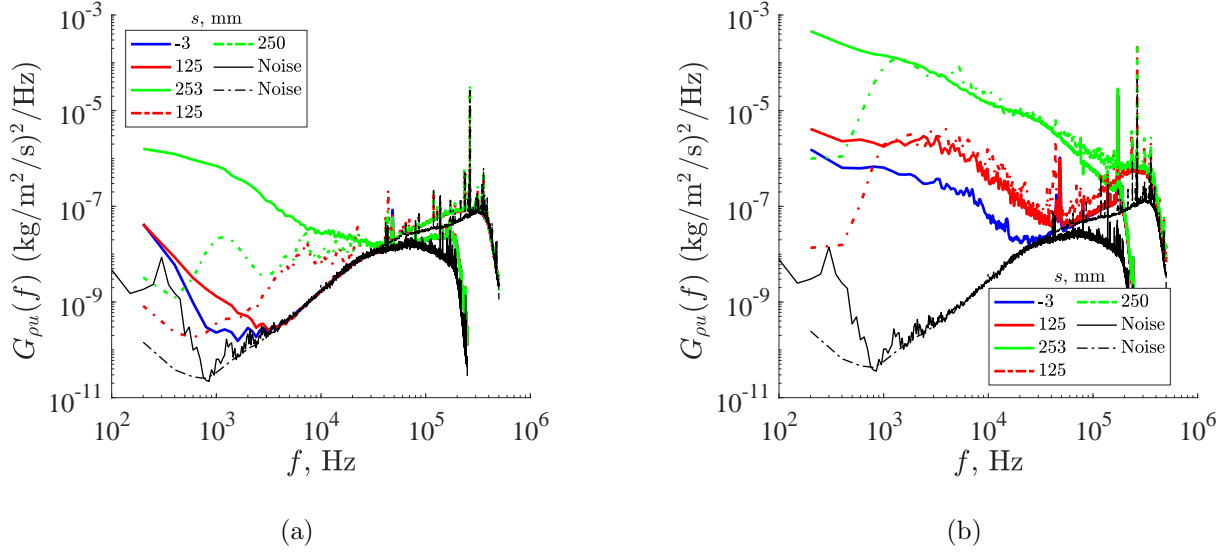
18

FIG. 7. Measured freestream and boundary-layer edge power spectra under quiet-flow conditions for select s locations: (a) $P_0 \approx 175$ kPa, and (b) $P_0 \approx 450$ kPa. Solid lines represent empty-tunnel freestream spectra and dashed lines represent boundary-layer edge spectra.

the electronic noise data will not be presented for subsequent power spectral plot to prevent clutter. For the data at $P_0 \approx 175$ kPa in figure 7(a), the solid lines show the empty-tunnel freestream data. Two features are observed in the empty-tunnel spectra. First, there is an increase in the low-frequency energy in terms of amplitude and bandwidth as s increases, albeit small. The mechanism responsible for this increase is not clear, but this behavior has been observed in our two-dimensional quiet nozzle as well.[19] Second, most of the rms energy is dominated by the f-squared noise of the anemometer that starts at $f \approx 2$ kHz for the most upstream location. The $\langle (\rho u)' \rangle$ values presented previously are dominated by this f-squared noise when the flow is quiet. The dashed lines in the figure represent the boundary-layer edge data (recall that these are high-passed filtered at 1 kHz and low-passed filtered at 400 kHz, compared to the freestream data that are high-passed filtered at 0.25 Hz and low-passed filtered at 200 kHz). The spectra in figure 7(a) at $s = 125$ mm have similar features except for greater spectral energy between approximately 2 to 20 kHz that is believed to be associated with the integrated-model traverse/probe system. A difference in the bandwidth of the low-frequency energy at $s \approx 250$ mm between the empty-tunnel and boundary-layer edge data is apparent and this difference is manifested in the observed increase of $\langle (\rho u)' \rangle$ in figure 6(a). Figure 7(b) shows a similar plot for the data at $P_0 \approx 450$ kPa. Similar features

are observed here. The main difference being the agreement between the empty-tunnel and boundary-layer edge spectra in the 2 to 20 kHz frequency band for locations at the start of measurements with the model traverse ($s = 125$ mm) because the high SNR in that frequency band as evident in the figure.

B. Cone baseline-flow measurements

The next step was to document carefully the mean-flow measurements and to compare the measurements with CFD results. The mean-flow data were acquired with both pitot-probe and hot-wire sensors.

1. Boundary-layer pitot-probe measurements

With the cone model installed in the tunnel, we started the process of aligning the cone axis to the incoming flow. This process involved obtaining boundary-layer pressure profiles at various ϕ and s locations. After several iterations of adjusting the cone, we settled on what we considered to be an acceptable alignment. Based on edge conditions of the pitot pressure profiles acquired at azimuthal positions 180° apart, the cone alignment for angles of attack and sideslip to the incoming flow were estimated to be within ±0.04°. The Mach-number profiles as derived from the measured pitot and surface static pressures are shown in figure 8(a) for different values of ϕ and s at $P_0 \approx 379.2$ kPa. The experimental data are plotted in Blasius similarity coordinates η ($= y\sqrt{Re_e/s}$) and are compared with the computed mean-flow profile at $s = 302$ mm. There is excellent agreement between the experimental data and CFD results except for locations near the wall and for $s = 125$ mm. The excellent degree of cone alignment with respect to pitch and yaw is clearly demonstrated in the plot by the data collapse. Additional Mach-number profiles over a range of P_0 and s are presented in figure 8(b). Both plots in figure 8 indicate a near self-similar profile with respect to location (s, ϕ) and Re_∞.

Preston tube measurements, P_p, at the surface were also made to investigate the laminar-to-turbulent transition state of the boundary layer. The pitot tube was traversed to a specified s location and then moved down to foul the probe onto the model surface. Preston tube data were acquired at this position before the probe was retracted and moved to the next
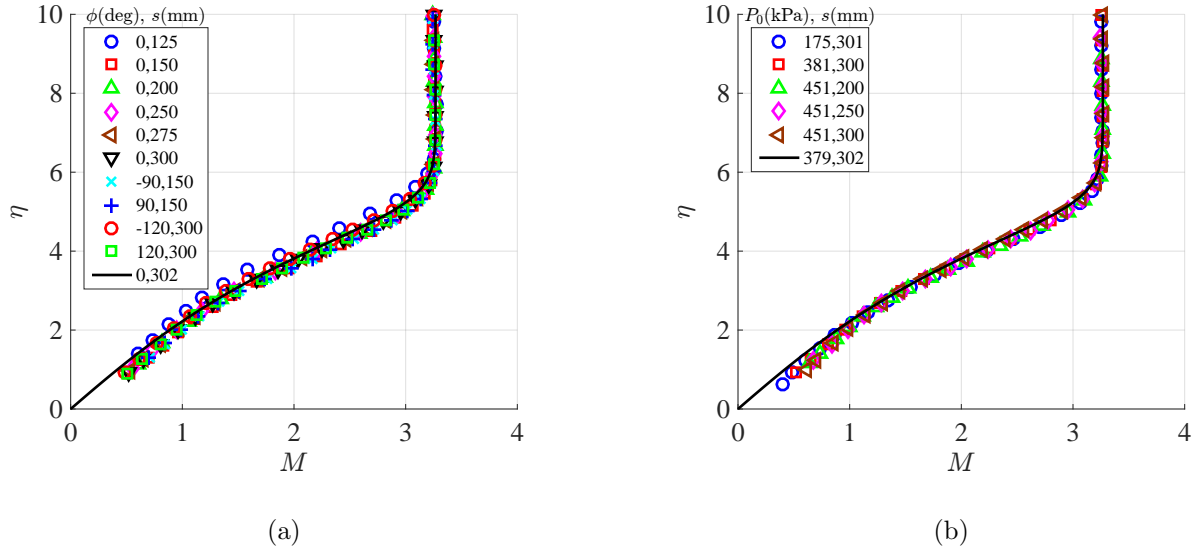
FIG. 8. Measured Mach-number profiles plotted in Blasius coordinates under quiet-flow conditions for: (a) different ϕ and s locations at $P_0 \approx 379.2$ kPa, and (b) different P_0 and s locations. The computed Mach-number profile at $s = 302$ mm is denoted by '——'.

s location. Preston tube data were acquired for a range of Re_∞ under quiet-flow conditions to include the maximum quiet-flow condition ($Re_\infty \approx 25.84 \times 10^6$ m^{-1} or $P_0 \approx 450$ kPa) and one noisy-flow condition ($Re_\infty \approx 13.89 \times 10^6$ m^{-1} or $P_0 \approx 242$ kPa). The unit Reynolds number for the noisy-flow condition was selected so that the onset of transition was located in the accessible s range. Figure 9 shows the normalized Preston tube data for a range of test conditions and azimuthal locations. For the noisy-flow condition (filled symbols), boundary-layer transition onset, as demonstrated by the increase in P_p/P_0, begins at $s_{tr} \approx 192$ mm. Meanwhile, for the quiet-flow condition (unfilled symbols), transition as measured by the mean-flow distortion is not realized; however, the data reported earlier by Chen, Malik, and Beckwith[7] and King[24] indicate that transition is imminent (note that $R^2 = 8.7 \times 10^6$ at $s = 300$ mm at the maximum Re_∞). Excellent azimuthal agreement is observed in the measured transition front for the noisy-flow condition in figure 9, which again demonstrates the degree of cone alignment as well as the cone-tip symmetry. The quiet-flow measurements also showed consistent results around the azimuth, i.e., no perceived transition onset.
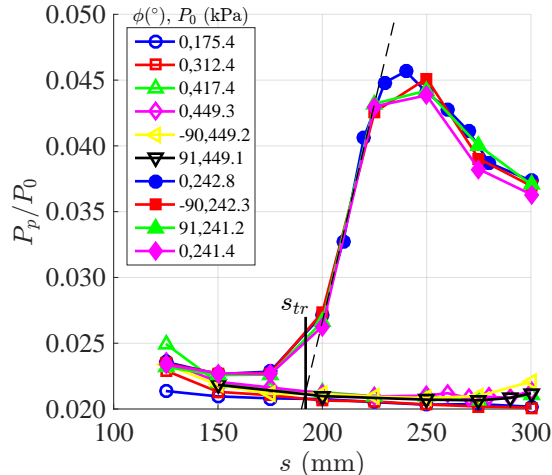
21

FIG. 9. Normalized Preston tube data (P_p/P_0) versus s. Filled symbols are for noisy-flow conditions and unfilled symbols are for quiet-flow conditions. The dashed black line represents an extrapolation of the transition data. The transition onset location (estimated as the intersection of the extrapolated dashed black line with the laminar data) is depicted by the solid black line.

2. Boundary-layer hot-wire measurements

Hot-wire and cold-wire boundary-layer measurements were acquired along the cone for a range of tunnel conditions. Reduced results in the form of mass flux and total temperature are shown in figure 10 for $P_0 \approx 379.2$ kPa. The measured profiles are plotted versus y for four s locations and are compared to the respective CFD results. Very good agreement is observed for the normalized mass-flux profiles in figure 10(a), particularly for the downstream profiles. The normalized temperature profiles are shown in figure 10(b). Good agreement is observed for the temperature profiles, but the temperature peaks are marginally overpredicted by the CFD results. These plots and findings are representative of the other test conditions.

C. Unsteady boundary-layer and stability measurements

1. Measurements in noisy flow

Unsteady boundary-layer measurements are first presented for the noisy-flow condition at $P_0 \approx 242.3$ kPa. The boundary layer transitioned from laminar to turbulent flow near the midsection of the cone. Mass-flux boundary-layer profiles were acquired at five streamwise
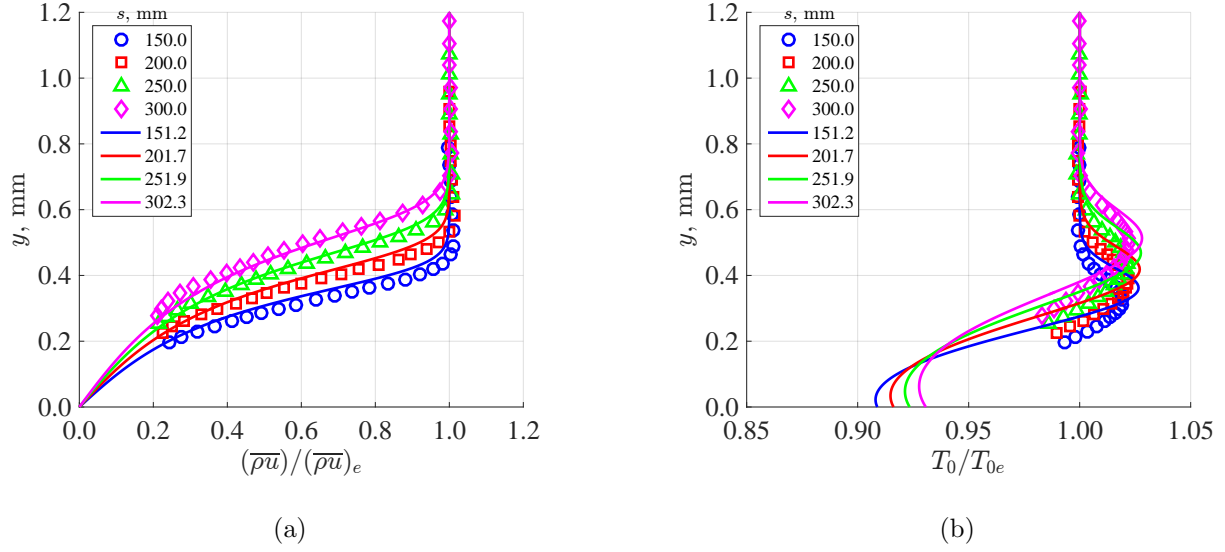
FIG. 10. Measured boundary-layer profiles in quiet flow for $\phi = 0°$ and $P_0 \approx 379.2$ kPa: (a) normalized $\overline{\rho u}$, and (b) normalized T_0. The computed mean profiles are denoted by lines.
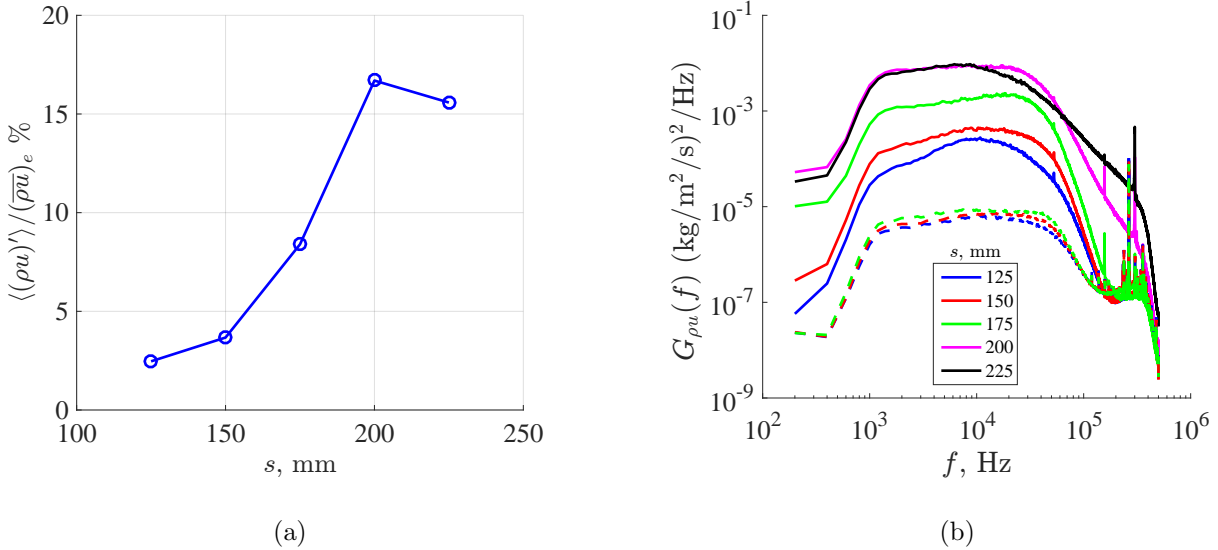

FIG. 11. Measured hot-wire data in noisy flow for $\phi = 0°$ and $P_0 \approx 242.3$ kPa: (a) maximum normalized broadband rms mass flux, and (b) power spectral density at maximum broadband y locations. Boundary-layer edge spectra at $y \approx 1$ mm for the first three s stations are included in plot as dashed lines.

locations along the cone surface from $s = 125$ to 225 mm. The maximum broadband rms mass flux at each s location is presented in figure 11(a). This maximum in $\langle(\rho u)'\rangle$ occurs near $\eta \approx 4.2$ to 4.6. The saturation location, $s \approx 200$ mm, in the figure gives an
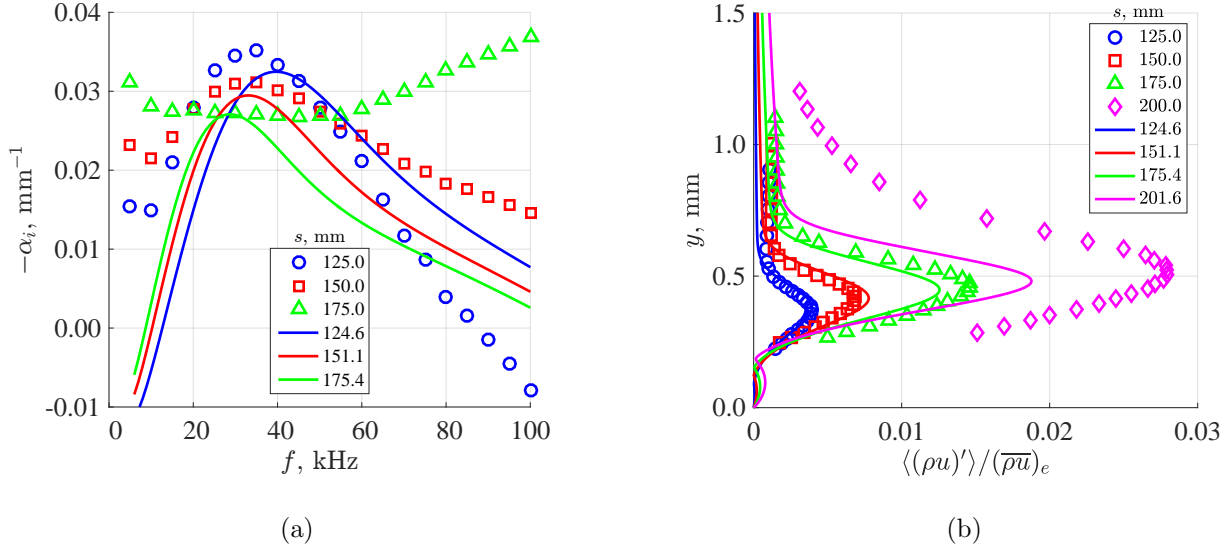
FIG. 12. Reduced hot-wire data in noisy flow compared with linear stability theory for $m = 20$ at $P_0 = 242.3$ kPa: (a) dimensional growth rates obtained from mass-flux growth, and (b) mode shapes at $f_c = 50$ kHz. The experimental data and LST results are denoted by symbols and lines, respectively.

indication of transition onset as measured from the unsteady data. This agrees to within our measurement resolution of s with the value ($s_{tr} \approx 192$ mm) obtained from the near-wall mean-flow distortion shown in figure 9. The corresponding N factor at transition from LST is $N \approx 3.9$ for $s_{tr} \approx 192$ mm. Saturation occurs when $\langle(\rho u)'\rangle/(\overline{\rho u})_e \approx 17\%$ at $s \approx 200$ mm. The corresponding power spectral densities at the maximum $\langle(\rho u)'\rangle$ are given in figure 11(b). Significant spectral broadening beyond $f \approx 100$ kHz is clearly evident at $s > 175$ mm. The plot also includes boundary-layer edge spectra for the $s = 125, 150,$ and 175 mm at $y \approx 1$ mm (largest acquired wall-normal location) in dashed lines. For locations of $s > 175$ mm, the peak lobe of the broadband rms mass-flux profile extended beyond the maximum measured y location. The boundary-layer edge spectra for the locations presented in the figure show very little change with increasing s, i.e., $\langle(\rho u)'_e\rangle/(\overline{\rho u})_e \sim 0.5\%$. The ratios of the maximum to the edge broadband rms mass flux at $s = 125, 150,$ and 175 mm are $\langle(\rho u)'\rangle/\langle(\rho u)'_e\rangle = 5.0,$ 6.6, and 13.4, respectively.

A plot of the growth rate versus frequency is presented in figure 12(a). The LST results are for an azimuthal wavenumber of $m = 20$ (corresponding to the most unstable mode from $s \approx 125$ to 200 mm). The measured $-\alpha_i$ at $s = 125$ mm compare favorably with the LST

growth rates. However, the comparison is very poor at $s = 175$ mm, particularly at the tails of the curve, where spectral broadening due to nonlinear effects are evident. Some degree of nonlinearity at the higher frequencies is believed to be present at $s = 150$ mm as well. The experimental maximum growth rates (in the vicinity of $f \approx 35$ kHz) follow the same trend as the predicted LST results, i.e., decreasing maximum growth rate with increasing s. The measured mode shapes at four measurement stations are presented in figure 12(b) for $f_c = 50$ kHz. The LST eigenfunctions for $f = 50$ kHz and $m = 20$ are scaled to match the measured peak value at $s = 125$ mm and this scale factor is used at the other streamwise locations. Good agreement is evident at the first two stations where the measured growth rates are in reasonable agreement with LST. For the two farther downstream stations, the LST mode shapes grossly underpredicts the measured data where the flow in nonlinear and the measured data include contributions for other azimuthal wavenumbers. Good-to-excellent agreement is realized for both the growth rates and mode shapes when the disturbances are small enough to preclude nonlinear effects.

2. *Measurements in quiet flow*

Next, we consider the unsteady boundary-layer measurements under quiet-flow conditions for $P_0 \approx 172.4$, 379.2, and 448.2 kPa. At a total pressure of $P_0 \approx 172.4$ kPa, no measurable instability above the electronic noise floor was discerned along the entire length of the cone (data not shown). Matlis[17] (see also Matlis and Corke[41]) made similar observations under quiet-flow conditions in the Mach 3.5 two-dimensional nozzle of the SLDT. Their measurements were acquired at a unit Reynolds number of 9.45×10^6 m^{-1} ($P_0 = 172$ kPa and $T_0 = 311$ K). For the purpose of this report, no further results are provided at this test condition. For that reason, we tested at the two higher total pressures. At total pressures of $P_0 \approx 379.2$ and 448.2 kPa, the results were found to be qualitatively similar to one another, except that the broadband rms mass fluxes at $s = 300$ mm are $\langle (\rho u)' \rangle / (\overline{\rho u})_e \approx 3.5$ and 6.4%, respectively. For that reason, both test conditions are discussed together.

A plot of the maximum growth amplitude at selected frequency bins versus s location is shown in figure 13(a) for $P_0 \approx 448.2$ kPa. The even values of f_c (10, 20, ..., 100) are not shown for clarity. The broadband growth amplitude (0-100 kHz) is also included in the figure. In general, the rms amplitudes decrease with increasing f_c at a given s location. The most-
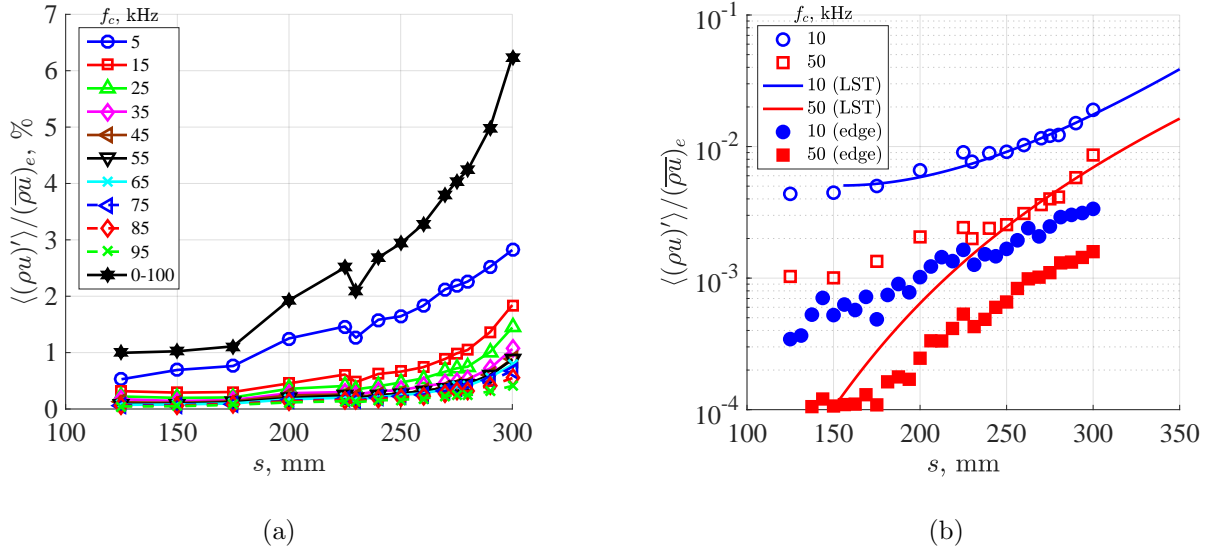
FIG. 13. Boundary-layer mass-flux growth under quiet-flow conditions at $P_0 \approx 448.2$ kPa: (a) normalized growth at selected f_c for the maximum measured mass flux, and (b) growth compared with LST at two values of f_c (edge mass flux denoted with filled symbols).

amplified first-mode instabilities predicted for $250 < s < 300$ mm by LST occur near $f = 50$ to 60 kHz and $m = 30$. The largest values of $\langle (\rho u)' \rangle$ throughout the measurement range do not coincide with the predicted most-amplified first-mode disturbances. To explore this further, we focused on two measured frequency bins: 1) a low-frequency bin ($f_c = 10$ kHz) with substantial amplitude and 2) a frequency bin ($f_c = 50$ kHz) within the LST-predicted most-amplified mode. Figure 13(b) presents the data for the maximum boundary-layer $\langle (\rho u)' \rangle$ and the edge $\langle (\rho u)'_e \rangle$, which are shown as unfilled and filled symbols, respectively. Note that the data up to $s \approx 180$ mm for $\langle (\rho u)'_e \rangle$ at $f_c = 50$ kHz are at the f-squared noise floor of the anemometer. Observe that the $\langle (\rho u)'_e \rangle$ for both the 10 kHz and 50 kHz forcing have similar streamwise growths for $s > 250$ mm. LST predictions in the form of e^N for $f = 10$ and 50 kHz and azimuthal wavenumber $m = 30$ for both frequencies are also included in figure 13(b). The LST results are scaled to match the respective measured data at $s = 260$ mm. The agreement between the measured $\langle (\rho u)' \rangle$ and e^N for 10 kHz is very good over the entire measurement range. This may lead one to suggest that the rms mass flux at 10 kHz is predominately driven by linear instability growth and not by the downstream external boundary-layer edge forcing $\langle (\rho u)'_e \rangle$. The measured $\langle (\rho u)' \rangle$ at 50 kHz compares reasonably well with the corresponding e^N for $s > 240$ mm and a similar speculation can be
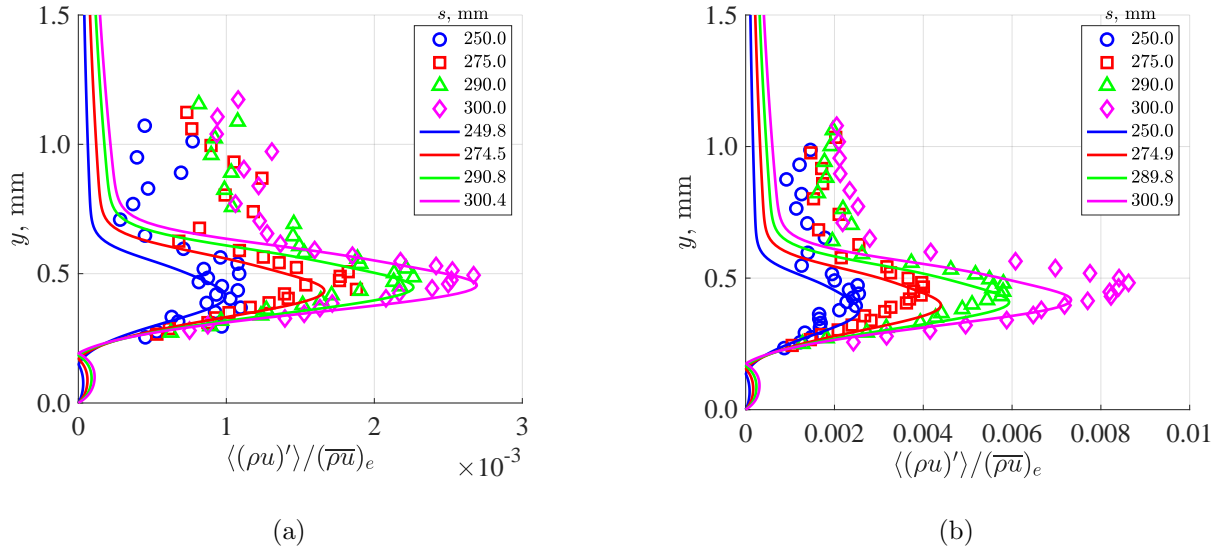
FIG. 14. Measured mode shapes under quiet-flow conditions and scaled eigenfunctions from LST ($f = 50$ kHz, $m = 30$): (a) $P_0 \approx 379.2$ kPa, and (b) $P_0 \approx 448.2$ kPa.

made here as for the 10 kHz measured instability.

The mode shapes for $P_0 \approx 379.2$ and 448.2 kPa are given in figure 14 along with the scaled LST eigenfunctions for $f = 50$ kHz and $m = 30$. The maximum values of the measured normalized mass flux are very small ($O(10^{-3})$), so the measured mode-shape profiles are relatively noisy. However, although the SNR is small, the mode shapes are clearly measurable at the latter measurement stations. The marginal SNR improvement in the mode shapes for $P_0 \approx 448.2$ kPa (figure 14(b)) versus $P_0 \approx 379.2$ kPa (figure 14(a)) is evident. The y locations of the peaks are slightly underpredicted by the LST eigenfunctions. The LST and measured mode-shape peaks are in good agreement for the range of streamwise stations for $P_0 \approx 379.2$ kPa in figure 14(a). As before, the LST and measured values are scaled to match at one location and the same scale factor is applied at the other locations. Similarly, the peaks of the LST and experimental mode shapes for $P_0 \approx 448.2$ kPa (figure 14(b)) agree reasonably well for all the streamwise locations except for the last station at $s = 301$ mm where the LST underpredicts the measured data. Next, the corresponding growth rates are presented in figure 15. The growth rates for $P_0 \approx 379.2$ kPa in figure 15(a) are overpredicted by LST for frequencies with higher growth rates. A similar plot for $P_0 \approx 448.2$ kPa is shown in figure 15(b). The measured $-\alpha_i$ for the first two measurement stations are again well below the LST predictions. As the SNR improved for the two latter stations ($s = 290$
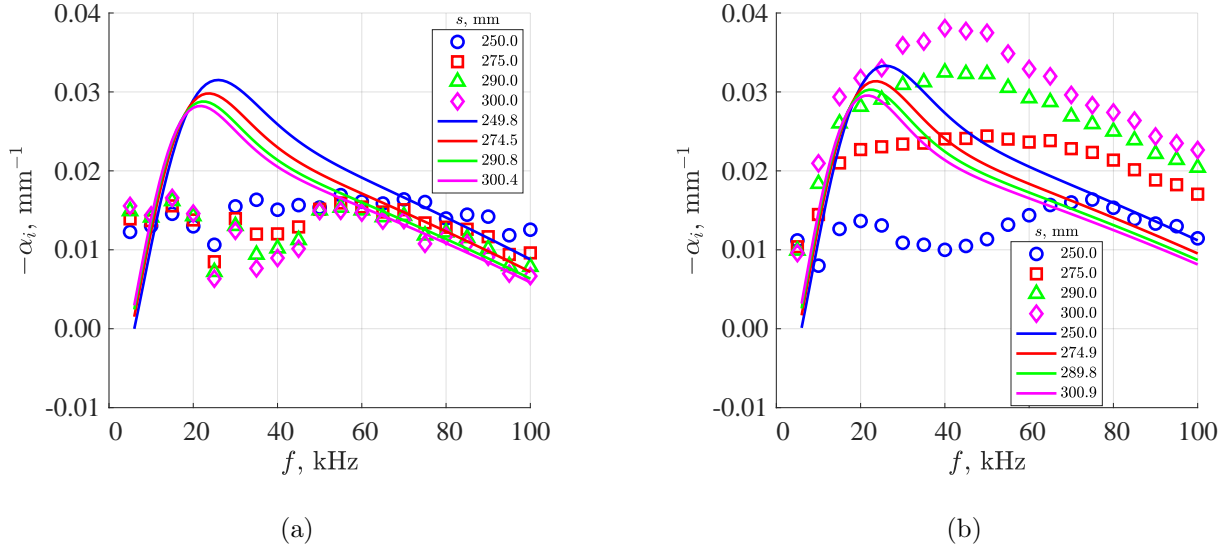
FIG. 15. Measured growth rates in quiet flow compared with LST ($m = 30$): (a) $P_0 \approx 379.2$ kPa, and (b) $P_0 \approx 448.2$ kPa.
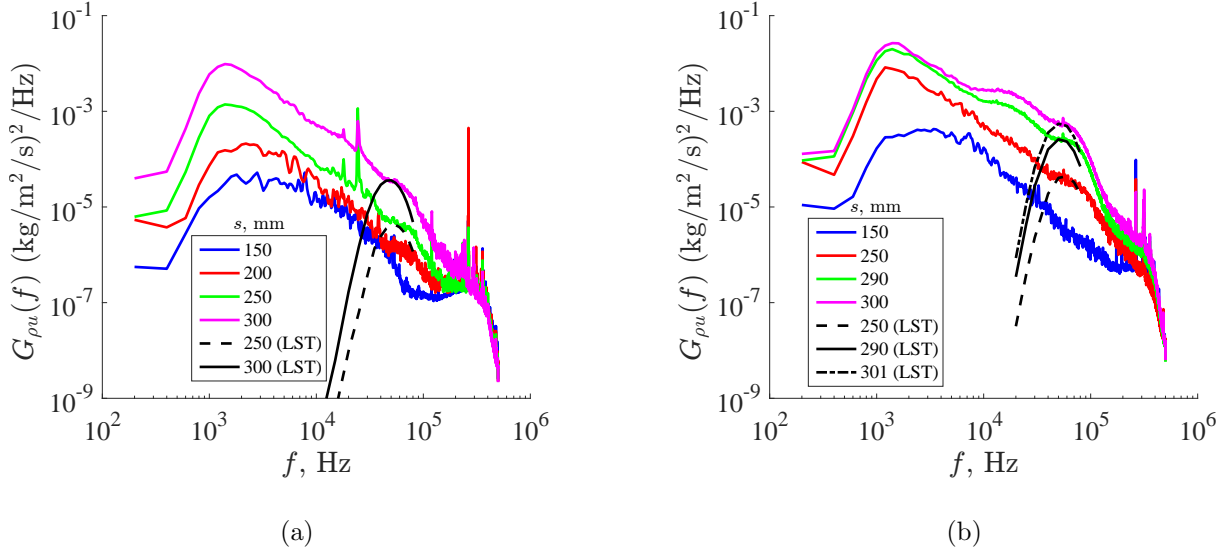

FIG. 16. Measured power spectra at the maximum $\langle (\rho u)' \rangle$ in quiet flow for select s locations: (a) $P_0 = 379.2$ kPa, and (b) $P_0 = 448.2$ kPa. LST results are shown for comparison.

and 300 mm), the growth rates are more akin to the LST predictions. The predictions underestimate the growth rates, peak frequencies, and frequency band, but the general features are fairly similar.

Finally, we consider the power spectral densities at the maximum broadband mass flux at selected s locations. Figure 16(a) shows the measured power spectral densities at four

streamwise locations for $P_0 \approx 379.2$ kPa. At the latter two measurement stations, a broad peak begins to emerge in the spectra. The scaled power spectra for e^N versus frequency of the most unstable first-mode disturbance are also plotted for the last two s stations. Excellent agreement with respect to frequency for the most unstable first-mode disturbance is observed between the measured spectra and the LST predictions. Similar results are presented for $P_0 \approx 448.2$ kPa in figure 16(b). The emergence of the most unstable first-mode instabilities is evident in the last three s stations. As before, excellent agreement is evident between the measured and predicted results. A low-frequency band (~ 20 kHz) is also evident in the last two measurement stations.

V.   DISCUSSION

The challenge in measuring naturally-occurring first-mode instabilities under quiet-flow conditions in a Mach-3.5 stream was clearly evident throughout this test campaign. However, similar hot-wire measurements by Lachowicz, Chokani, and Wilkinson,[42] Blanchard and Selby,[43] Rufer,[44] and Hofferth et al.[45] have been acquired at Mach 6 under quiet-flow conditions for naturally-occurring second-mode instabilities on cones. Their results not only clearly demonstrated the presence of second-mode instabilities and harmonics but demonstrated the dominance of these second-mode instabilities in the transition process. The most-amplified instabilities at hypersonic speeds are two-dimensional (2-D) second-mode waves ($m = 0$), but for supersonic Mach numbers, the most-amplified instabilities are three-dimensional (3-D) first-mode waves with large values of the azimuthal wavenumber (typically $m > 10$). This raises a few fundamental questions:

1. What is the relative efficiency of the receptivity process in generating the 2-D versus 3-D most-amplified instability waves in a low-noise wind tunnel?

2. How are the 3-D first-mode disturbances with large m generated near the leading-edge region of the cone, where the circumference gets vanishingly small?

3. Are the inherent difficulties of such measurements at moderate to high supersonic Mach numbers due to the significantly lower first-mode amplitude ratios realized at Mach 3.5 versus the much larger second-mode amplitude ratios at Mach 6 (refer to computations by Mack[8])?

Most of these are vexing questions to resolve experimentally, due in part to the current state-of-the-art measurement capabilities, i.e., the inability to acquire temporally- and spatially-resolved measurements with noise floor levels 2 to 3 orders of magnitude lower than hot-wire anemometry. Under quiet-flow conditions, our measured signal amplitudes were extremely small and could be smaller than or on the same order of magnitude as the anemometer f-squared noise ($O(10^{-5})$ to $O(10^{-4})$). Additionally, we know in general that the total measured mass flux within the boundary layer included both the forced response due to the freestream/boundary-layer edge excitation and the instability (free) response predicted by stability theory. Mack[15] has shown that the peak value of the forced response can be 5 – 20 times as large as the freestream value without any instability amplification. When both the forced and instability responses were comparable, the measured mass-flux values were difficult to interpret. With our current measurements, we are unable to estimate the relative importance of the forced and instability responses, i.e., the relative magnitude and phase between the forced response and instability response are unknown. However, DNS (direct numerical simulations) computations in conjunction with carefully conducted experiments may help to resolve these questions/issues.

So why are our measured low-frequency disturbance amplitudes (e.g., $f_c = 10$ kHz) so dominant relative to disturbance amplitudes (e.g., $f_c = 50$ kHz) within the predicted most-amplified first-mode frequencies (see figure 13(b))? Here, we consider only the data acquired at the highest Re_∞ ($P_0 \approx 448.2$ kPa). At 10 kHz, LST predicts an amplification of $e^N \sim 4$ from the branch I location ($s \approx 155$ mm) to the last measurement location ($s = 300$ mm). But at 50 kHz, LST predicts amplification of $e^N \sim 4.4 \times 10^3$ from the branch I location ($s \approx 45$ mm) to $s = 300$ mm. The measured boundary-layer edge disturbances and maximum boundary-layer disturbances for 10 kHz at its branch I location are both within our measurement capability (see figures 7(b) and 16(b) for spectra at $s = 125$ and 150 mm, respectively). In contrast, the measured freestream and boundary-layer edge disturbances at 50 kHz near its branch I location are below the anemometer noise floor (see figure 7(b) for spectra at $s = -3$ and 125 mm). For that matter, boundary-layer edge spectra (data not shown) indicate that the energy at 50 kHz is below the anemometer noise floor for all locations upstream of $s \approx 180$ mm, and this is borne out in figure 13(b). The measured maximum boundary-layer disturbances at 50 kHz at our most upstream location $s = 125$ mm indicate that our measured values were above the anemometer noise floor (see spectra at

$s = 150$ mm in figure16(b)); however, we do not know the relative importance of the forced versus instability responses in the measured mass flux.

Given the aforementioned information with respect to our measurement limitations, we conjecture the following scenario based on the measurements. We can assume that the freestream power-spectral component at 50 kHz is approximately 2 orders of magnitude less than the component at 10 kHz—based on the extrapolation of the precipitous spectral rolloff with frequency (see the spectrum at $s = -3$ mm in figure 7(b)). With that assumption, the freestream/edge spectral amplitude component at 50 kHz is $O(10^{-5})$. If the receptivity coefficient at the branch I location ($s \approx 45$ mm) is $O(10^0)$, then we would expect amplitude measurements based on an amplification of $e^N \sim 4.4 \times 10^3$ to be $O(10^{-2})$ or spectral power of $O(10^{-4})$. Interestingly, this $O(10^{-4})$ in spectral power agrees with our measurements at $s = 300$ mm (see figure16(b)). So referring back to figure 13(b) where $\langle(\rho u)'\rangle/(\overline{\rho u})_e \sim O(10^{-2})$ at $s = 300$ mm, we can speculate based on LST that $\langle(\rho u)'\rangle/(\overline{\rho u})_e \sim 2 \times 10^{-6}$ at branch I ($s \approx 45$ mm) in the boundary layer, i.e., below current measurement capability.

Our measurements suggest that the flow was not measurably receptive to the external disturbances that impinged on the latter portion of the cone surface. This was shown by the fact that the measured mass flux followed the LST disturbance growth at 10 kHz and 50 kHz throughout that impingement region (refer to figure 13(b)). Previous DNS computations by Balakumar[36] predicted that the receptivity location is near the nose region on a smooth cone surface. Chen, Malik, and Beckwith[7] tested a 5° half-angle cone under quiet-flow conditions with the cone tip located at two streamwise locations (7.6 mm apart). They concluded that the cone boundary layer is much more sensitive to the wind-tunnel noise in the vicinity of branch I than farther downstream, since they measured lower transition Reynolds numbers at the lower Re_∞ for the downstream cone location. However, the data show that for the higher Re_∞ conditions, where the branch I location is expected to move upstream, the transition Reynolds numbers are consistent at both cone locations. The recent DNS by Balakumar et al.[25] for our test condition mimicked the measured freestream noise in our experiment at different frequencies, convection speeds, and azimuthal wavenumbers. First, the forced responses of the boundary-layer flow over the cone were computed and the eigenfunctions of the instability modes based on LST were compared to the forced eigenfunctions. The forced responses for the low azimuthal wavenumbers were larger than the responses for the high wavenumbers. For an incident acoustic angle of 65° from the normal to the incoming

flow, the ratio of maximum amplitudes inside and outside the boundary layer is about 4 and 1.4 for $m = 0$ and $m = 30$, respectively. The simulations with 2-D and 3-D forcing at 10 kHz and 50 kHz for low and high m values did not show any observable instability wave response from the downstream external forcing. The results showed that the maximum ρu fluctuations inside the boundary layer generally followed the local fluctuations at the edge of the boundary layer. The DNS results[25] suggest that the observed boundary-layer disturbances were primarily a local response of the boundary layer to the external forcing at the boundary-layer edge and not an instability response. The DNS[25,36] and experimental[7] results all support our finding here that the boundary-layer was not measurably receptive to the impinging acoustic freestream noise on the latter portion of the cone, well downstream of branch I locations.

Good agreement for large SNR data was observed for the noisy-flow condition. For the noisy-flow data, the exponential growth of the instability response is expected to overwhelm the forced response; thus, the measured mode shape approximated the LST eigenfunction, provided that the instabilities were still linear. Even at the first measurement station $R \approx$ 1395, the comparison was excellent. For the same reason, the resulting measured growth rates compared reasonably well to the LST growth rates. As nonlinearity developed, both the growth rates and mode shapes deviated from linear theory, with the growth rate being more sensitive to the degree of nonlinearity (see figure 12). For the quiet-flow data, the results depended on the SNR, with improved results for larger SNRs. No consistent measurable results above the noise floor were obtained for $P_0 \approx 172.4$ kPa, even at the last measurement station of $R \approx 1826$, and this was consistent with findings of Matlis and Corke.[41] For the larger Re_∞ conditions ($P_0 \approx 379.2$ and 448.2 kPa), the relative magnitude and phase between the forced response and instability response are unknown. The source of any discrepancies between the measured mode shapes and eigenfunctions in figure 14 may be the result of the aforementioned unknowns, the relatively low SNR, and wavenumber contributions of the measured results. Computations[25] showed that the peaks in the eigenfunctions for the forced response were found to occur at a slightly larger η than the peaks for the linear stability response and the shapes were different near the lower part of the boundary layer. Similar features were observed between the DNS eigenfunction results for the nonuniform 3-D acoustic forcing and the eigenfunctions from linear stability and these can be observed to some level in figure 14 for the data with larger SNR. Similarly, the measured growth

rates in figure 15 suffer the same limitations. Both sets of results show improvement as the SNR and the instability response increased for the higher Re_∞ condition, where the measurements ranged from $R \approx 2688$ to 2945.

We were unable to obtain transition under quiet-flow conditions for this test. The maximum Re_∞ of the test was conducted just below the quiet-flow limit, and the extent of the streamwise travel was limited to $s = 300$ mm. Based on this information, we know that the transition N factor is greater than 8.5 in quiet flow. We cannot say definitively which frequencies are ultimately responsible for breakdown, but the evidence up to the last measurement station suggests that spectral energy at frequencies below the predicted most-amplified band are likely dominant to that point. Spectral energy at the most-amplified first-mode instabilities predicted by LST began to emerge in the power spectral densities at downstream locations as shown in figure 16. The most-amplified LST instabilities in this figure are for azimuthal wavenumbers ranging from $m = 25$ to 35. It should be noted that we did not have the ability to independently measure m or the wave angle ψ in this test entry. Recent unforced measurements in a conventional facility by Wu and Radespiel[18] on a 7° half-angle cone at Mach 3 estimated $\psi \approx 45°$ compared to 65° from linear theory.

Finally, the need to measure the freestream and/or boundary-layer edge unsteady disturbances was clearly evident throughout this study. By carefully interrogating the freestream and boundary-layer edge conditions, evidence of low-frequency disturbances, albeit small, were present in the freestream/edge flow. The receptivity of the boundary-layer flow to these freestream conditions evidently provided the initial conditions for the boundary-layer instability disturbances. Stetson et al.[46] commented on the need to document these low-frequency disturbances found in the wind-tunnel freestream environment, and the different role they play in high-speed transition measurements with planar versus conical geometries.

VI. SUMMARY

A transition-to-turbulence study was conducted at $M_\infty = 3.5$ in the NASA Langley Supersonic Low-Disturbance Tunnel for a transitioning boundary layer on a 7° half-angle cone. All measurements were acquired with a naturally-occurring wind-tunnel environment operating in either a quiet (low-disturbance) mode or noisy (conventional) mode. Extreme care was taken throughout the study to reduce measurement noise sources and uncertainties and

to document the flow and environmental conditions, all with the aim of avoiding ambiguous results. Hot-wire anemometry was employed for our unsteady measurements, which were calibrated to respond primarily to mass flux. Complementary mean-flow solutions and linear stability analyses were computed for the nominal test conditions to support the experimental findings and further detail analysis can be found in a companion paper.[25] We demonstrated that good agreement under noisy-flow conditions between experimental stability measurements and computed linear stability results can be achieved. To the authors' knowledge, we are the first to successfully measure the most-amplified first-mode instabilities as predicted by linear theory in a naturally-occurring, low-noise environment. These measurements at moderate-to-high supersonic Mach numbers have been elusive in past studies, partly due to the low signal levels of the measured quantities. The initial conditions of the unstable disturbances were provided by the freestream environment, and this receptivity process was primarily confined to the leading-edge portion and branch I locations of the cone. The dominant disturbances under quiet conditions were at frequencies well below those predicted by linear theory within our measurement window, and the disturbances grew based on linear theory. Future measurement techniques with reduced inherent noise levels that can provide temporally- and spatially-resolved data are desirable for such studies. DNS using the measured freestream condition (spatial distribution and spectral content) as an initial condition can be used to better understand the receptivity process and reconcile the relative importance between the forced and unstable boundary-layer responses.

VII.   ACKNOWLEDGEMENTS

REFERENCES

[1]O. Reynolds, "An experimental investigation of the circumstances which determine whether the motion of water shall be direct or sinuous, and of the law of resistance in parallel channels," Philosophical Transactions of the Royal Society London **174**, 935–982 (1883).

[2]M. V. Morkovin, "Critical evaluation of transition from laminar to turbulent shear layers with emphasis on hypersonically traveling bodies," Tech. Rep. AFFDL-TR-68-149 (Wright-Patterson Air Force Base, 1969).

[3]A. V. Fedorov, "Receptivity of a high-speed boundary layer to acoustic disturbances," Journal of Fluid Mechanics **491**, 101–129 (2003).

[4]J. Laufer, "Aerodynamic noise in supersonic wind tunnels," Journal of the Aerospace Sciences **28**, 685–692 (1961).

[5]S. R. Pate and C. J. Schueler, "Radiated aerodynamic noise effects on boundary-layer transition in supersonic and hypersonic wind tunnels," AIAA Journal **7**, 450–457 (1969).

[6]S. P. Schneider, "Effects of high-speed tunnel noise on laminar-turbulent transition," Journal of Spacecraft and Rockets **38**, 323–333 (2001).

[7]F.-J. Chen, M. R. Malik, and I. E. Beckwith, "Boundary-layer transition on a cone and flat plate at Mach 3.5," AIAA Journal **27**, 687–693 (1989).

[8]L. M. Mack, "Boundary-layer stability theory," Tech. Rep. JPL-900-277-Rev-A (also NASA-CR-131501) (Jet Propulsion Laboratory, 1969).

[9]J. Laufer and T. Vrebalovich, "Stability and transition of a supersonic laminar boundary layer on an insulated flat plate," Journal of Fluid Mechanics **9**, 257–299 (1960).

[10]J. M. Kendall, "Supersonic boundary layer stability," in *Boundary Layer Transition Study Group Meeting* **2**, edited by W. D. McCauley (U.S Air Force Report No. BSD-TR-67-213, 1967) pp. 10.1–10.8.

[11]J. M. Kendall, "Wind tunnel experiments relating to supersonic and hypersonic boundary-layer transition," AIAA Journal **13**, 290–299 (1975).

[12]A. Demetriades, "Growth of disturbances in a laminar boundary layer at Mach 3," Physics of Fluids A **1**, 312–317 (1989).

[13]A. D. Kosinov, A. A. Maslov, and S. G. Shevelkov, "Experiments on the stability of supersonic laminar boundary Layers," Journal of Fluid Mechanics **219**, 621–633 (1990).

[14]P. Graziosi and G. L. Brown, "Experiments on stability and transition at Mach 3," Journal of Fluid Mechanics **472**, 83–124 (2002).

[15]L. M. Mack, "Linear stability theory and the problem of supersonic boundary-layer transition," AIAA Journal **13**, 278–289 (1975).

[16]T. C. Corke, D. A. Cavalieri, and E. H. Matlis, "Boundary-layer instability on sharp cone at Mach 3.5 with controlled input," AIAA Journal **40**, 1015–1018 (2002).

[17] E. H. Matlis, *Controlled experiments on instabilities and transition to turbulence on a sharp cone at Mach 3.5*, Ph.D. thesis, University of Notre Dame, Notre Dame, IN (2003).

[18] J. Wu and R. Radespiel, "Investigation of instability waves in a Mach 3 laminar boundary layer," AIAA Journal **53**, 3712–3725 (2015).

[19] M. A. Kegerise, L. R. Owens, and R. A. King, "High-speed boundary-layer transition induced by an isolated roughness element," AIAA Paper 2010-4999 (2010).

[20] M. A. Kegerise, R. A. King, L. R. Owens, M. Choudhari, A. Norris, F. Li, and C.-L. Chang, "An experimental and numerical study of roughnes-induced instabilities in a Mach 3.5 boundary layer," RTO-AVT-200/RSM-030 (2012).

[21] M. A. Kegerise, R. A. King, M. Choudhari, F. Li, and A. Norris, "An experimental study of roughness-induced instabilities in a supersonic boundary layer," AIAA Paper 2014-2501 (2014).

[22] L. R. Owens, M. A. Kegerise, and S. P. Wilkinson, "Off-body boundary-layer measurement techniques development for supersonic low-disturbance flows," AIAA Paper 2011-284 (2011).

[23] G. Beeler, S. P. Wilkinson, P. Balakumar, and K. McDaniel, "Crossflow instability on a wedge-cone at Mach 3.5," AIAA Paper 2012-2825 (2012).

[24] R. A. King, "Three-dimensional boundary-layer transition on a cone at Mach 3.5," Experiments in Fluids **13**, 305–314 (1992).

[25] P. Balakumar, R. A. King, A. Chou, L. R. Owens, and M. A. Kegerise, "Receptivity and Forced Response to Acoustic Disturbances in High-Speed Boundary Layers," AIAA Journal **56**, 510–523 (2018).

[26] F.-J. Chen, M. R. Malik, and I. E. Beckwith, "Advance Mach 3.5 axisymmetric quiet nozzle," AIAA Paper 90-1592 (1990).

[27] I. E. Beckwith, T. R. Creel, F.-J. Chen, and J. M. Kendall, "Free-stream noise and transition measurements on a cone in a Mach 3.5 pilot low-disturbance tunnel," NASA TP-2180 (1983).

[28] A. J. Smits, K. Hayakawa, and K. C. Muck, "Constant temperature hot-wire anemometer practice in supersonic flows – Part 1: The normal wire," Experiments in Fluids **1**, 83–92 (1983).

[29] L. S. Kovásznay, "The hot-wire anemometer in supersonic flow," Journal of the Aeronautical Sciences **17**, 565–572 (1950).

[30] J. Laufer and R. McClellan, "Measurements of heat transfer from fine wires in supersonic flows," Journal of Fluid Mechanics **1**, 276–289 (1956).

[31] C. F. Dewey, "A correlation of convective heat transfer and recovery temperature data for cylinders in compressible flow," International Journal of Heat and Mass Transfer **8**, 245–252 (1965).

[32] W. Behrens, "Total temperature thermocouple probe based on recovery temperature of circular cylinder," International Journal of Heat and Mass Transfer **14**, 1621–1630 (1971).

[33] P. Balakumar, H. Zhao, and H. Atkins, "Stability of hypersonic boundary-layers over a compression corner," AIAA Paper 2002-2848 (2002).

[34] P. Balakumar, "Transition in a supersonic boundary layer due to acoustic disturbances," AIAA Paper 2005-96 (2005).

[35] P. Balakumar, "Boundary layer receptivity due to roughness and freestream sound for supersonic flows over axisymmetric cones," AIAA Paper 2008-4399 (2008).

[36] P. Balakumar, "Receptivity of supersonic boundary layers due to acoustic disturbances over blunt cones," AIAA Paper 2007-4491 (2007).

[37] R. A. King and K. S. Breuer, "Acoustic receptivity and evolution of two-dimensional and oblique disturbances in a Blasius boundary layer," Journal of Fluid Mechanics **432**, 69–90 (2001).

[38] R. A. King and K. S. Breuer, "Oblique transition in a laminar Blasius boundary layer," Journal of Fluid Mechanics **453**, 177–200 (2002).

[39] M. Nishioka and M. V. Morkovin, "Boundary-layer receptivity to unsteady pressure gradients: experiments and overview," Journal of Fluid Mechanics **171**, 219–261 (1986).

[40] W. S. Saric, "Low-speed boundary-layer transition experiments," in *Transition experiments, theory computations*, edited by T. C. Corke, G. Erlebacher, and M. Y. Hussaini (Oxford, 1994) pp. 1–114.

[41] E. H. Matlis and T. C. Corke, "Quantitative hot-wire measurements in supersonic boundary layer," FEDSM2003-45080 (2003).

[42] J. T. Lachowicz, N. Chokani, and S. P. Wilkinson, "Boundary-layer stability measurements in a hypersonic quiet tunnel," AIAA Journal **34**, 2496–2500 (1996).

[43] A. E. Blanchard and G. V. Selby, "An experimental investigation of wall-cooling effects on hypersonic boundary-layer stability in a quiet wind tunnel," NASA CR-198287 (1996).

[44]S. J. Rufer, *Hot-wire measurements of instability waves on sharp and blunt cones at Mach 6*, Ph.D. thesis, Purdue University, West Lafayette, IN (2005).

[45]J. Hofferth, W. Saric, J. Kuehl, E. Perez, T. Kocian, and H. Reed, "Boundary-layer instability and transition on a flared cone in a Mach 6 quiet wind tunnel," International Journal Engineering Systems Modelling and Simulation **5**, 109–124 (2013).

[46]K. F. Stetson, R. L. Kimmel, E. R. Thompson, J. C. Donaldson, and L. G. Siler, "A comparision of planar and conical boundary layer stability and transition at a Mach number of 8," AIAA Paper 91-1639 (1991).